Lecture 7. More on BL wind profiles and turbulent eddy structures

In this lecture…

- Stability and baroclinicity effects on PBL wind and temperature profiles

- Large-eddy structures and entrainment in shear-driven and convective BLs.

Stability effects on overall boundary layer structure

Above the surface layer, the wind profile is also affected by stability. As we mentioned previously, unstable BLs tend to have much more well-mixed wind profiles than stable BLs. Fig. 1 shows observations from the Wangara experiment on how the velocity defects and temperature profile are altered by BL stability (as measured by H/L). Within stability classes, the velocity profiles collapse when scaled with a velocity scale u_* and the observed BL depth H, but there is a large difference between the stability classes.

Baroclinicity

We would expect baroclinicity (vertical shear of geostrophic wind) to also affect the observed wind profile. This is most easily seen for a laminar steady-state Ekman layer in a geostrophic wind with constant vertical shear $\mathbf{u}_g(z) = (G + Mz, Nz)$, where $M = -(g/fT_0)\partial T/\partial y$, $N = (g/fT_0)\partial T/\partial x$. The momentum equations and BCs are:

$$-f(v - Nz) \qquad = \nu \, d^2u/dz^2$$

$$f(u - G - Mz) \; = \nu \, d^2v/dz^2$$

$$u(0) = 0, u(z) \sim G + Mz \; \text{ as } z \to \infty.$$

$$v(0) = 0, v(z) \sim Nz \; \text{ as } z \to \infty.$$

The resultant BL velocity profile is the classical Ekman layer with the thermal wind added onto it.

$$u(z) = G(1 - e^{-\zeta} \cos \zeta) + Mz, \tag{7.1}$$

$$v(z) = G \, e^{-\zeta} \sin \zeta + Nz. \quad (\zeta = z/\delta_E, \delta_E = (2\nu/f)^{1/2}) \tag{7.2}$$

The added linear shear drives a height-independent viscous momentum flux which affects the surface stress but does not perturb the vertical convergence of the momentum flux.

The added contribution of the thermal wind can considerably alter the BL wind profile. Fig. 7.2 shows example wind hodographs with $M = 0$ and N positive, zero, and negative. The near-surface wind is slightly more turned toward the surface low pressure to the north. The largest crossing angle of the surface wind direction across the surface isobars (aligned along the x-axis) occurs if $M < 0, N > 0$, corresponding to surface cold advection. This effect is clearly seen in Fig. 7.3, showing average crossing angle vs. thermal wind orientation in 23000 wind profiles over land (Hoxit 1974). On weather maps, one can see much larger crossing angles behind cold fronts than ahead of them. On the other hand, the wind turns less with height if $N > 0$ (surface cold advection). The effect is stronger in the late afternoon (00Z) than the early morning (12Z) soundings. This is because during the day, convection allows more vigorous mixing of air from significant height down close to the surface, allowing the thermal wind to have a stronger effect.

Garratt
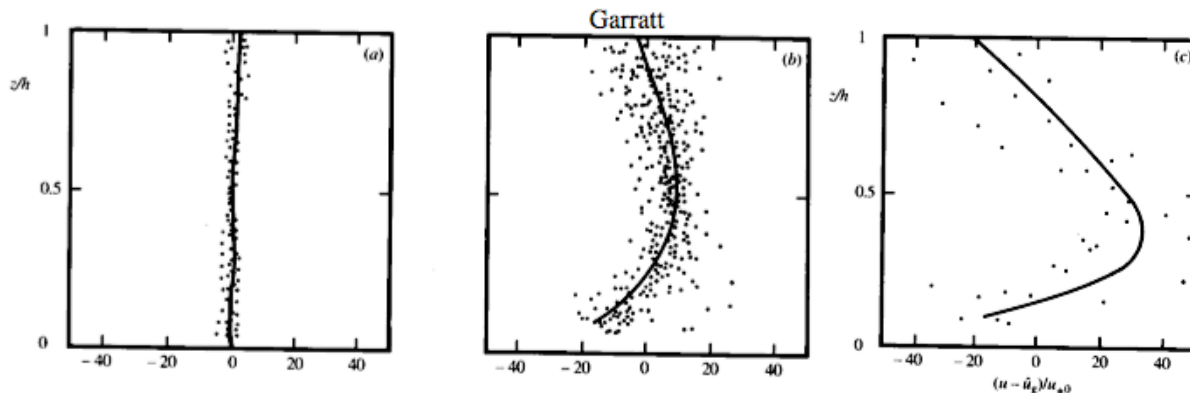
Fig. 3.13 Profiles of the normalized velocity defect for the *u*-component as a function of normalized height z/h, based on Eq. 3.82 and an analysis of Wangara observations. Three stability regimes are presented: (a) $-150 < h/L < -120$; (b) $0 < h < 30$; (c) $180 < h/L < 210$. Curves are drawn by eye. After Yamada (1976), *Journal of Atmospheric Sciences*, American Meteorological Society.
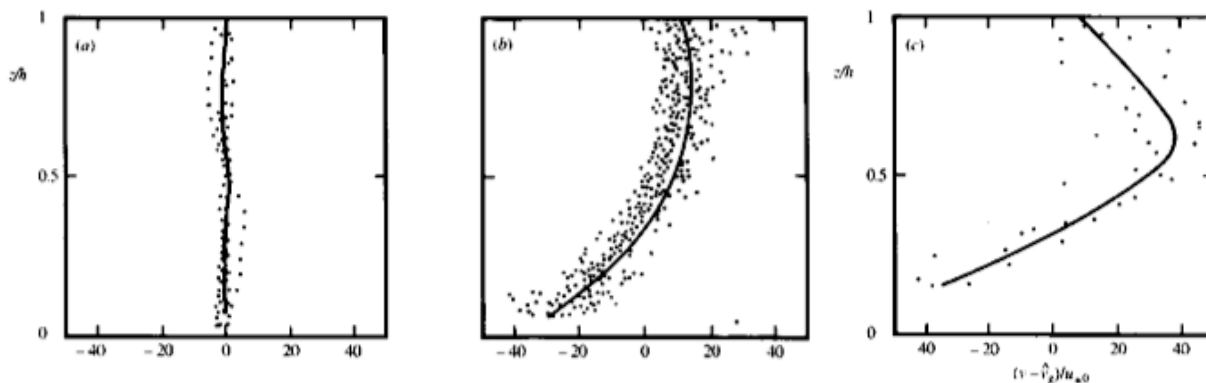
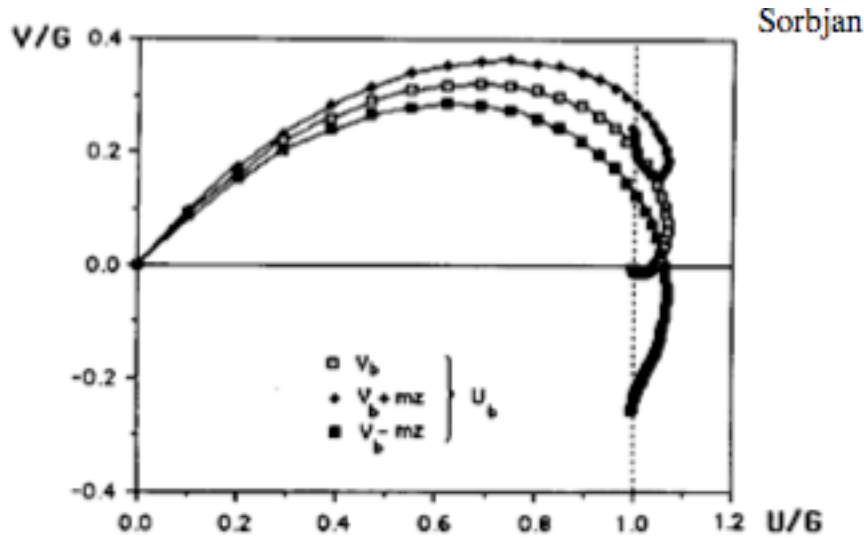As above, except for *v*.
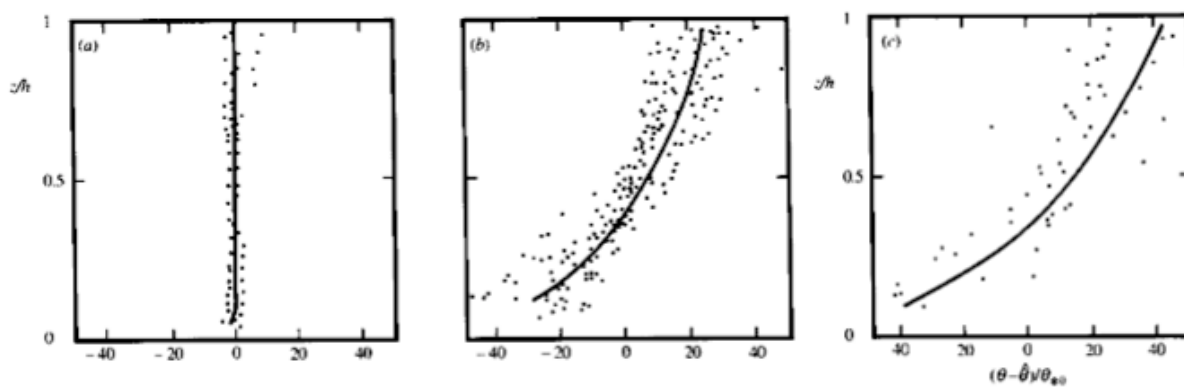
As above, except for θ. Here $\hat{\theta}$ is the BL-mean θ.

Fig. 7.1: Scaled ageostrophic velocity and potential temperature profiles in convective ($h/L \ll 0$), neutral ($h/L \approx 0$) and unstable ($h/L \gg 0$) boundary layers. Here h (H in text) is the BL depth and L the Obukhov length. Note relative well-mixedness of the unstable profiles.

Figure 6.11 Ekman spirals obtained for the baroclinic correction of the V component of the wind velocity, $a = 0.001$, $m = 0.0001$. Points are plotted every 100 m, starting on the surface. U_b, V_b-barotropic components of the wind vector. Dotted line shows directions of the thermal wind vectors.

Fig. 7.2: Ekman spirals for thermal wind with $M = 0$ and $N > 0$, $N = 0$ (no thermal wind), $N < 0$. Near-surface wind is oriented more in $+y$ direction (larger crossing angle) for $N > 0$.
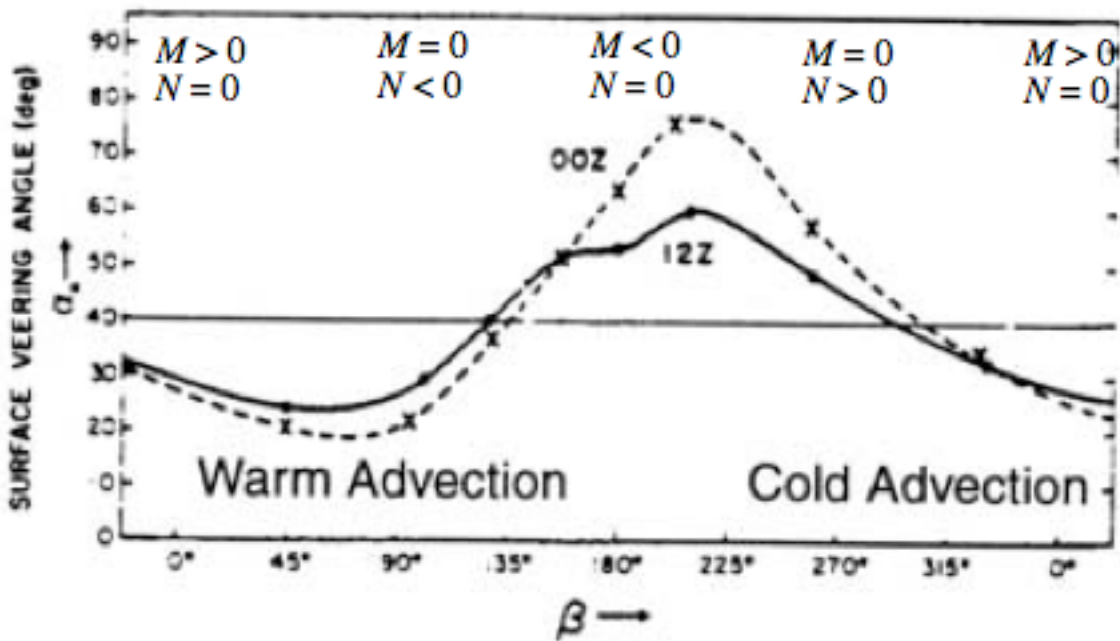

Fig. 7.3: Isobaric crossing angle of surface wind vs. angle of thermal wind. Afternoon (00 Z) soundings show stronger effect due to stronger vertical mixing in a more convective BL (Hoxit 1974).

Turbulent Eddy Structures, Turbulence Profile, and Entrainment (Garratt 3.3)

For applications such as dispersion of pollutants, it is important to understand the characteristics of turbulence in different BL types. LES simulations illustrate some of these characteristics. Most of the figures below are from Moeng and Sullivan (1994, *JAS*, **51**, 999-1022).

Neutral BLs: Streaks in surface layer

Moeng and Sullivan simulated a neutral BL capped by a strong (8 K) inversion at a height $z_i = $ 500 m (for consistency with their figures, we will follow their notation rather than using H for BL height). The geostrophic wind is 15 m s^{-1} in the +x direction and $u_* = 0.5$ m s^{-1}. Figure 7.4 shows x-y slices of u' at various heights, and the wind hodograph. Because of the trapping of the turbulence by the capping inversion, the wind shear within the bulk of the BL is fairly small (nearly a mixed layer), with strong wind shear across the inversion.

We can see that at the top of the surface layer ($z/z_i = 0.1$), u' is organized in **streaks**, long cylindrical eddies or `rolls' oriented about 20° to the left of the geostrophic wind. The wind perturbations weaken and become less linearly organized with height.   The figure below shows an x-z cross section of u', w', and $u'w'$ across the center of the domain in y. Here one can see the strong negative correlation between u' and w' (updrafts have a smaller u than downdrafts), especially for $z/z_i < 0.5$. In fact, the correlation coefficient between u' and w' is -0.4 at below this level. This downward momentum flux is what maintains the near-surface wind against the strong surface drag.

Weakly Unstable BLs: Rolls mixing the entire BL

Moeng and Sullivan also simulated a weakly unstable boundary layer similar to their neutral case, but with a surface heat flux of 50 W m^{-2}, giving an Obukhov length $L = -200$ m comparable to H. In this case (Fig. 7.5), the streaky structure is still apparent at the lowest levels, but large convective rolls dominate the turbulence higher in the BL and help keep it well-mixed. The buoyant and shear contributions to TKE are comparable in this case. A **convective velocity** scale based on surface buoyancy flux can be derived from the TKE equation.

$$w_* = (B_0 H)^{1/3}, \tag{7.3}$$

for this case $w_* = 0.9$ m s^{-1} (Note that $H/L = -kw_*^3/u_*^3$, connecting back to the stability classes at the beginning of this lecture).

Convective BLs

Lastly, let's look at a purely buoyancy-driven or convective BL. The simulations shown (Moeng and Rotunno 1990, JAS) are below a rigid boundary and do not include entrainment, but do show the overall structure well. At the bottom, there is a very good correlation between w¥ and q¥, with polygonal regions of updraft separating circular patches of downdraft. As we move close to the BL top, the updrafts accelerate and combine to become circular, and the temperature fluctuations become much less well correlated with the updrafts. For penetrative convection, in fact the updrafts would be a bit cooler than the surrounding air at the highest level shown.
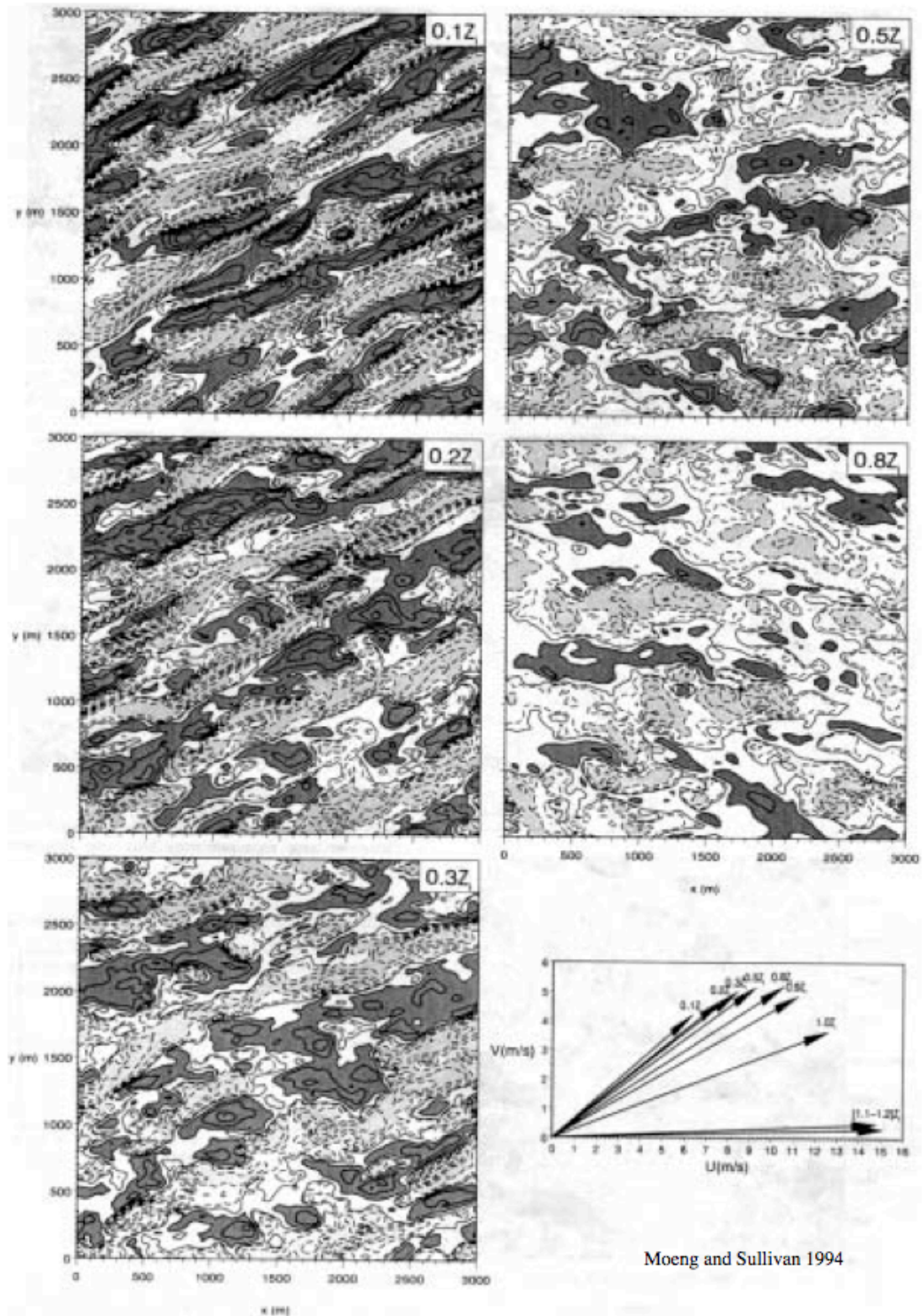
FIG. 3. Contours of u in the x–y plane at five height levels for simulation S and its wind hodograph: contours (−3, −2.5, −2, −1.5, −1, −0.5, −0.1, 0.1, 0.5, 1, 1.5, 2, 2.5), dark (light) shading values larger (smaller) than 0.5 (−0.5).

Fig. 7.4: Horizontal sections of u' in a shear-driven PBL under a strong inversion.
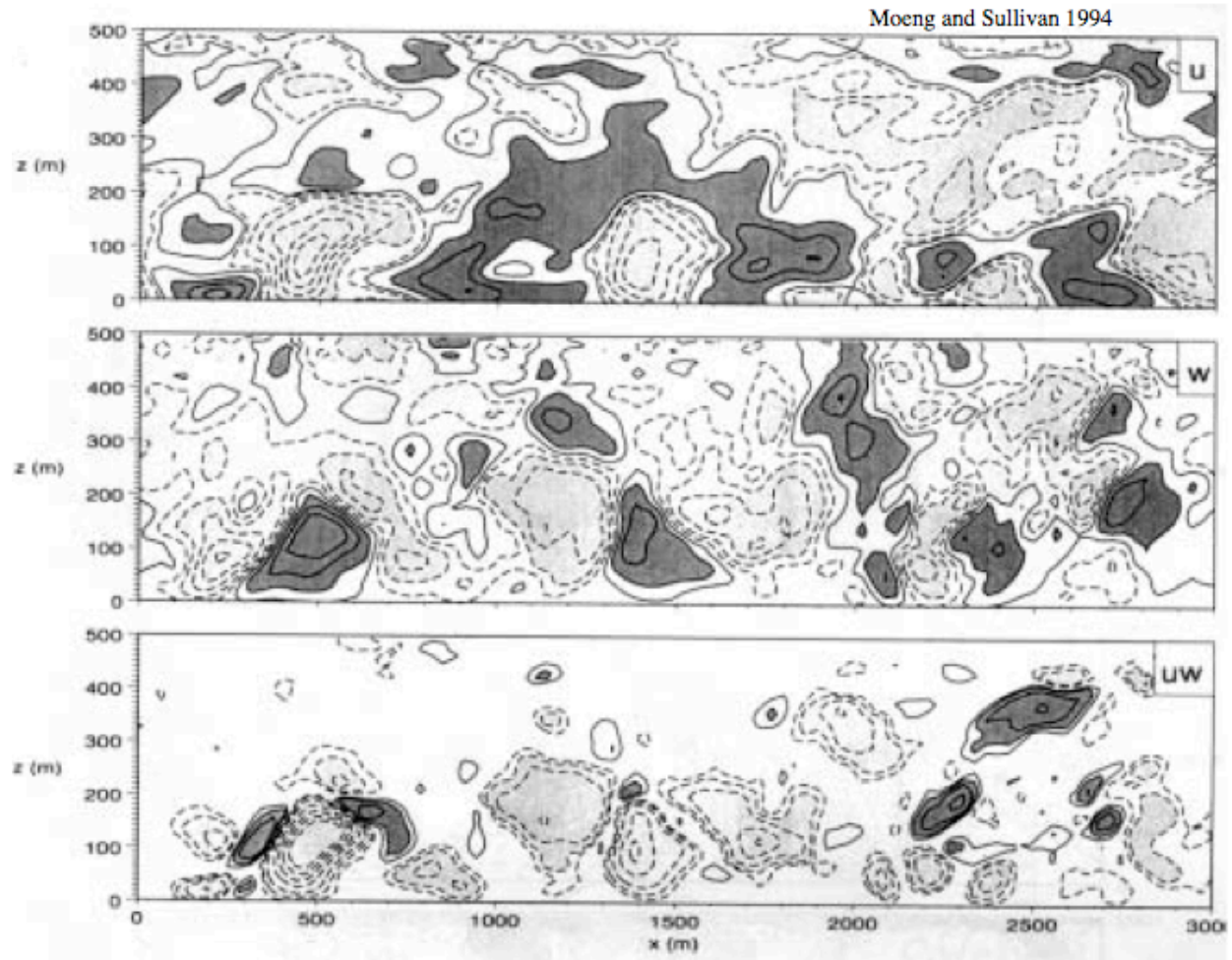
Fig. 7.5: Vertical sections of u', w' and $u'w'$ in a shear-driven BL under a strong inversion. Note strong anticorrelation of u', w' ($u'w' < 0$) in the lower half of the BL.
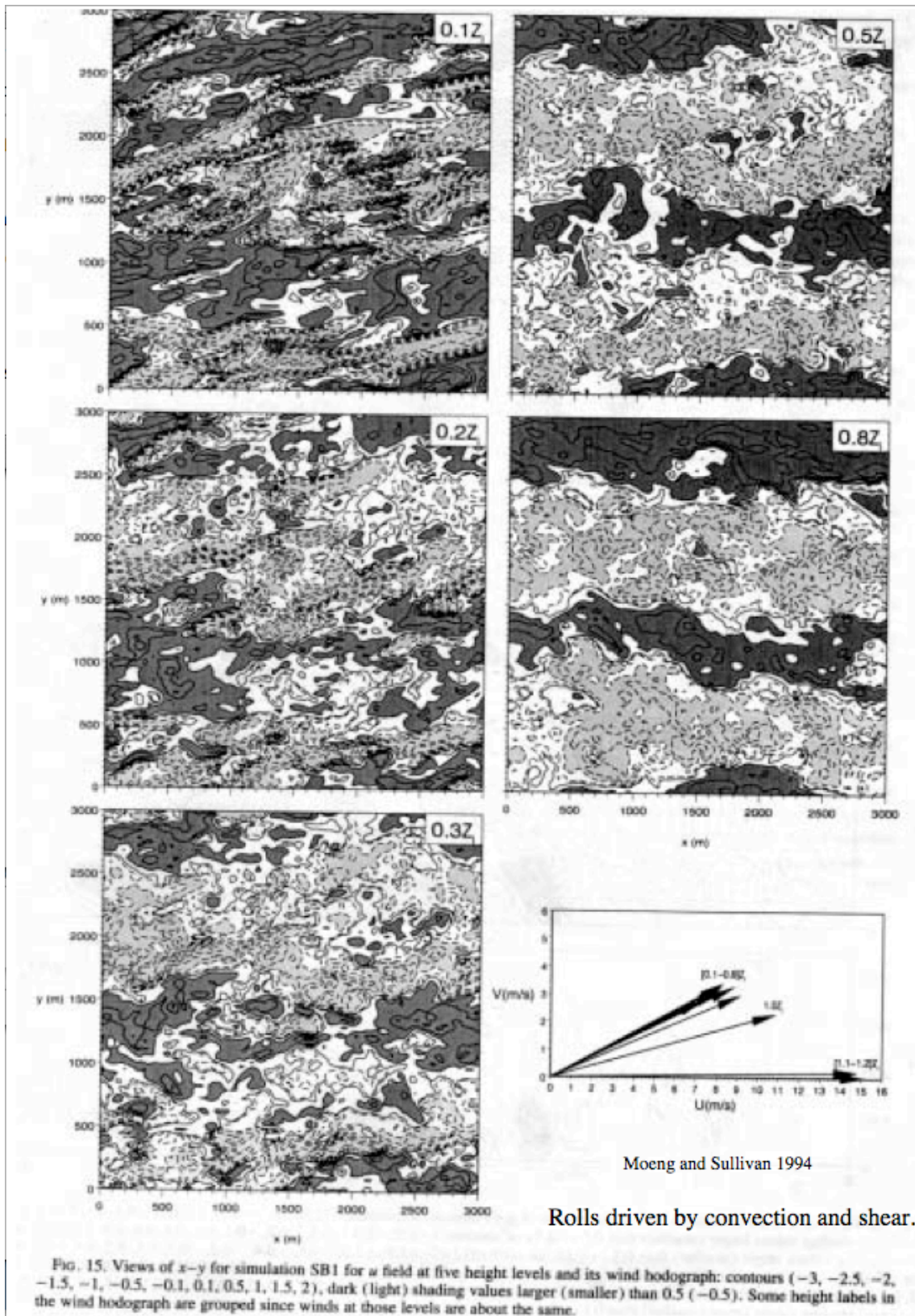
FIG. 15. Views of x–y for simulation SB1 for w field at five height levels and its wind hodograph: contours (−3, −2.5, −2, −1.5, −1, −0.5, −0.1, 0.1, 0.5, 1, 1.5, 2), dark (light) shading values larger (smaller) than 0.5 (−0.5). Some height labels in the wind hodograph are grouped since winds at those levels are about the same.

Fig. 7.6: As in Fig. 7.4, but with an added 50 W m^{-2} surface heat flux.

Pure convective BL **w**   Moeng and Rotunno 1990   T-T̄

At
Z=0.9

At
Z=0.5

At
Z=0.1

A

B

C

D

FIG. 8. As in Fig. 3, except for Experiment H. Vertical cross sections through the
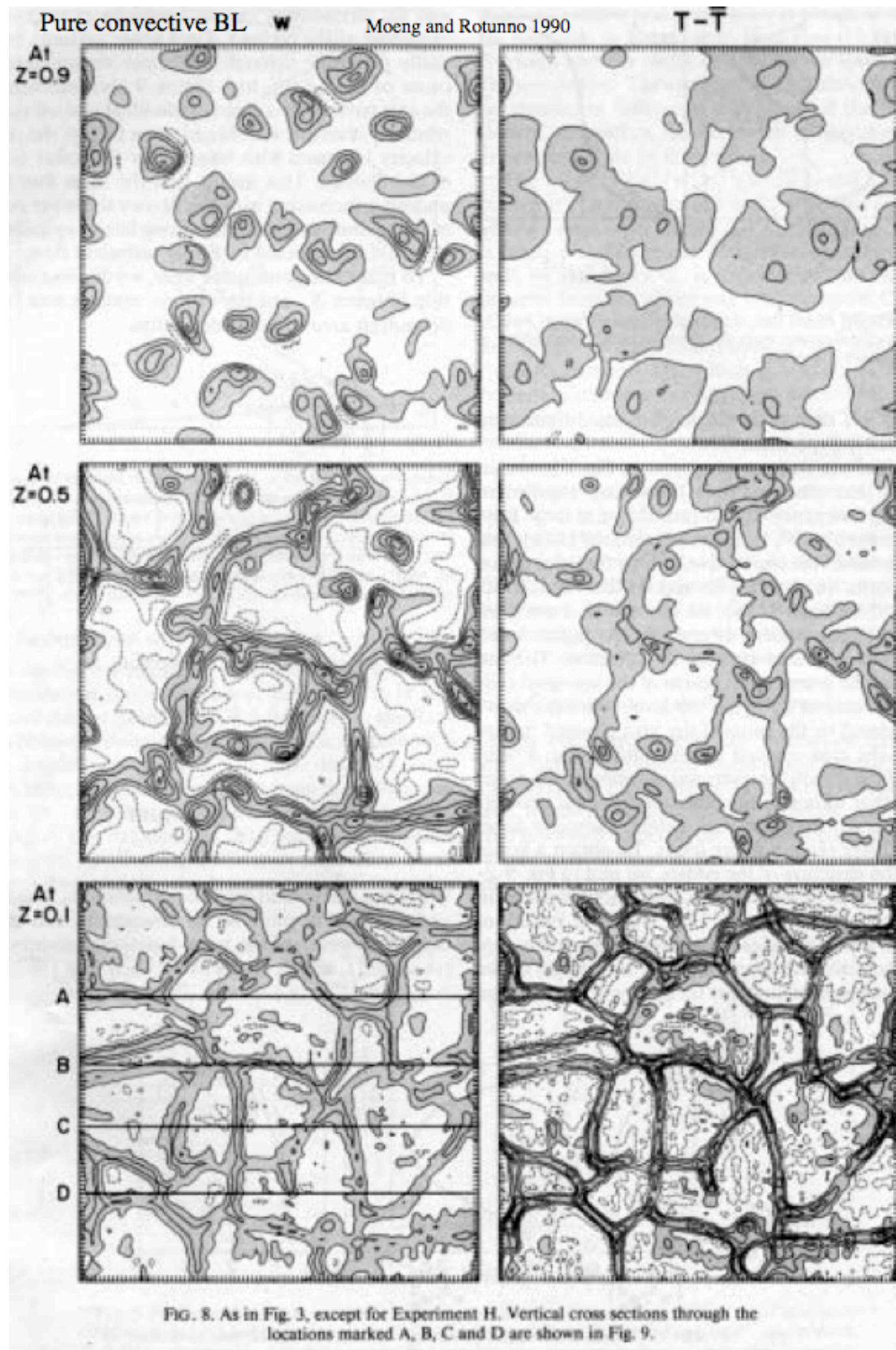locations marked A, B, C and D are shown in Fig. 9.

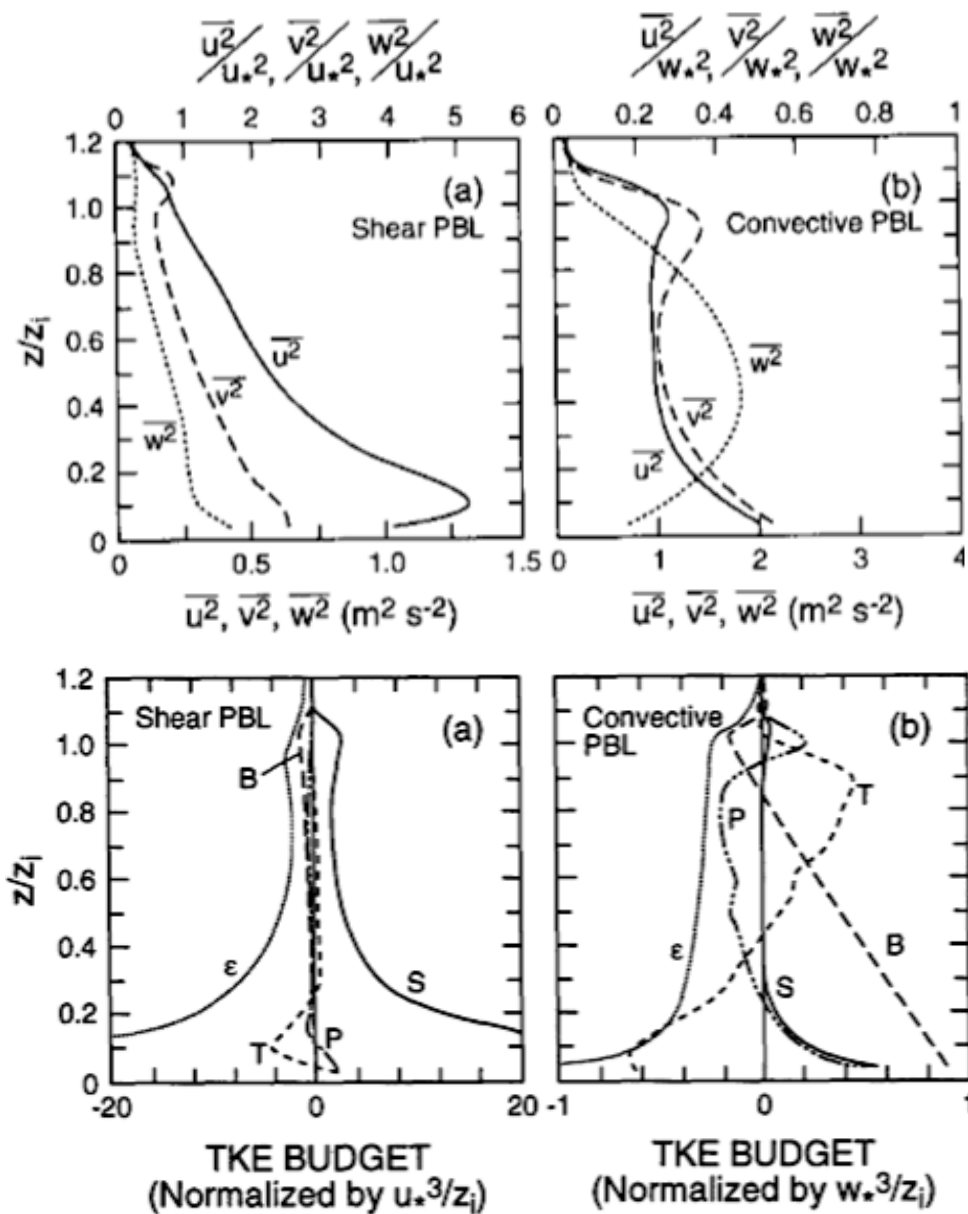Fig. 7.7: Horizontal sections of u' and w' through a convective BL

Fig. 7.8: Velocity variance profiles (top) and TKE budgets (bottom) for shear-driven and
     convective BLs under strong inversion.

Turbulent velocity variance profiles

Fig. 7.8 shows the vertical profiles of the variances of the three velocity components and the
TKE budgets for a shear-driven and convective BL.   For a shear-driven BL, the velocity
variances are all strongest near the ground, with the strongest perturbations in *u* at all levels. As
we have discussed already, the TKE budget is essentially a balance between shear production
(most of which occurs in the lowest 20% of the BL where shear and momentum fluxes are both
largest) and turbulent dissipation, with little contribution from turbulent transport. However, at

the inversion ($z/z_i = 1$), about 1/3 of the shear production of TKE is going into consumption by buoyancy fluxes associated with entrainment of potentially warm air from above the inversion.

For a convective BL, the velocity variances show a very different structure than for a shear-driven BL. They are dominated by the large eddies, which have updrafts in the middle of the BL and predominantly lateral motions at its top and bottom. There is much more velocity variance in the upper part of the BL.

Although the main source of TKE is buoyancy production and this is largest near the surface, the TKE dissipation rate is almost uniform with height and equal to $0.4w_*^3/z_i$. TKE is fluxed upward (T) and created in the inversion by pressure work (P). Again, about 1/3 of the TKE fluxed into the inversion drives negative buoyancy production and 2/3 drives dissipation.

Entrainment

Fig. 7.9 shows an LES-simulated time sequence of vertical sections (Sullivan et al. 1998, JAS) of the top of a convective BL penetrating a moderate inversion of 4 K. Note the undulations in the BL top, with a tongue of dark, partly mixed, downward moving air getting *entrained* - sucked into the BL, on the edge of an updraft-induced hummock. In addition to incorporating non-turbulent air from above the inversion into the boundary layer, entrainment is associated with a downward buoyancy flux $\overline{w'b'}_i$ at the inversion, because it brings down warm air ($b'>0$) in downward-moving tongues ($w' < 0$).

For a pure dry-convective BL this flux is about $-0.2w_*^3/z_i = -0.2B_0$ (Fig. 7.8b).   In the shear-driven simulation, Fig. 7.8a shows $\overline{w'b'}_i = -u_*^3/z_i$. One caveat is that this result might be sensitive to the ratio z_i/L, which will affect how strong the shear-driven turbulence is near the top of the boundary layer compared to near the surface.   By interpolating between these simulations and the weakly convective simulation in Fig. 7.6, Moeng and Sullivan arrived at an empirical form for the entrainment buoyancy flux atop a dry, sheared convective boundary layer,

$$\overline{w'b'}_i = -0.2w_m^3/z_i \qquad w_m^3 = 5u_*^3 + w_*^3 \tag{7.4}$$

Since the TKE of the entraining eddies is supplied from below, so we expect the entrainment buoyancy flux to be intimately tied to the TKE budget within the boundary layer.
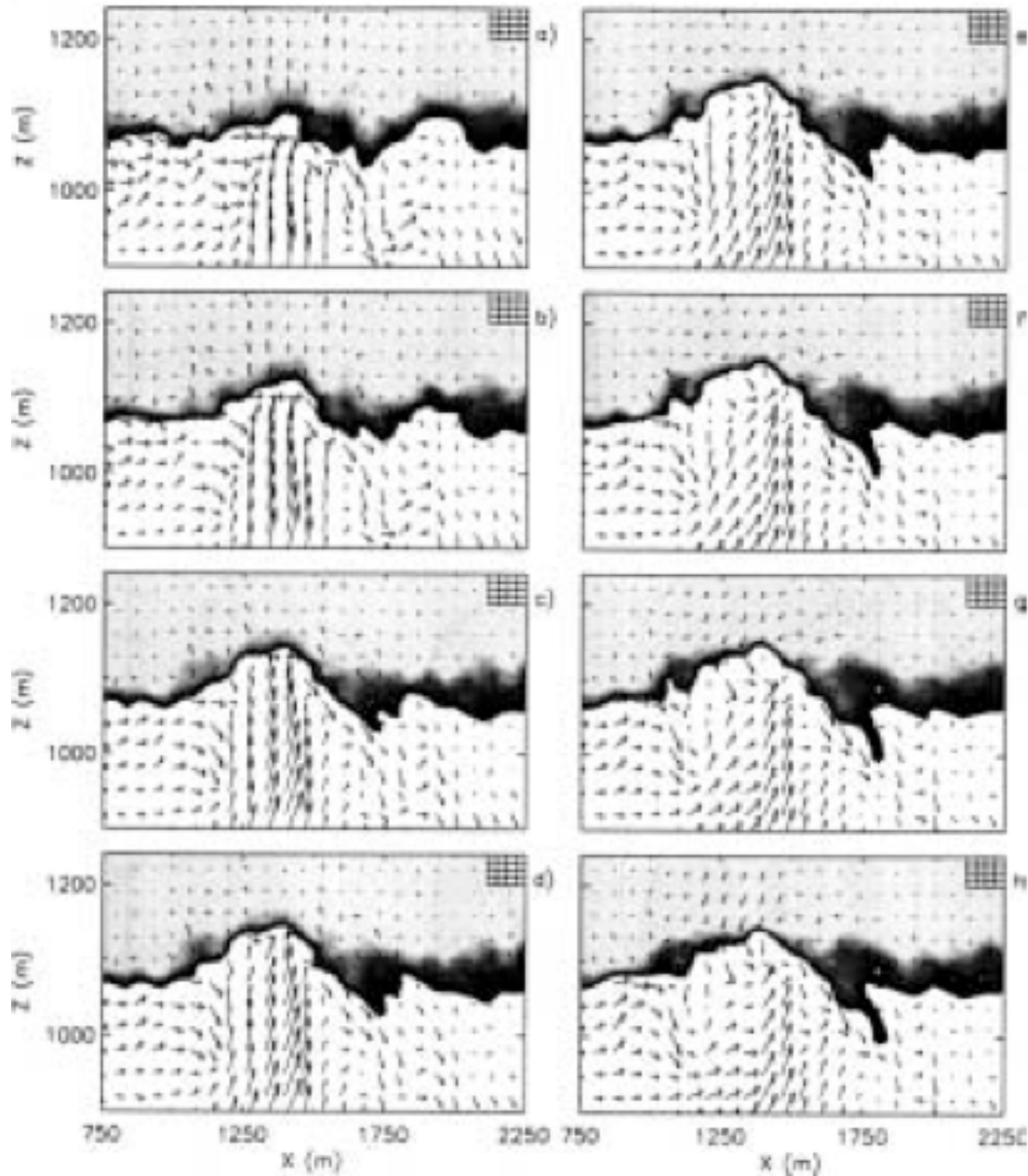
Fig. 7.9: Time sequence of cross-sections 10 s apart through an LES entrainment event at the top of a convective BL. Arrows indicate velocity in the *x-z* plane. White indicates $\theta < 304$ K (BL air), other shades from black to light grey show increasing θ up to the free-tropospheric value of 308 K. Hence, the darker shaded region indicates partly mixed air with potential temperatures intermediate between the BL and free-tropospheric values, The black tongue going into the BL at *x* = 1750 is being entrained into the BL. . Grid resolution is shown at top right of each plot. From Sullivan et al. (1998).